# Effect of Mg and Sr Additions on the Formation of Intermetallics in Al-6 Wt Pct Si-3.5 Wt Pct Cu-(0.45) to (0.8) Wt Pct Fe 319-Type Alloys

F.H. SAMUEL, P. OUELLET, A.M. SAMUEL, and H.W. DOTY

Al-Si alloys are materials that have been developed over the years to meet the increasing demands of the automotive industry for smaller, lighter-weight, high-performance components. An important alloy in this respect is the 319 alloy, wherein silicon and copper are the main alloying elements, and magnesium is often added in automotive versions of the alloy for strengthening purposes. The mechanical properties are also ameliorated by modifying the eutectic silicon structure (strontium being commonly employed) and by reducing the harmful effect of the $\beta$-$Al_5FeSi$ iron intermetallic present in the cast structure. Magnesium is also found to refine the silicon structure. The present study was undertaken to investigate the individual and combined roles of Mg and Sr on the morphologies of Si, $Mg_2Si$, and the iron and copper intermetallics likely to form during the solidification of 319-type alloys at very slow (close to equilibrium) cooling rates. The results show that magnesium leads to the precipitation of $Al_8Mg_3FeSi_6$, $Mg_2Si$, and $Al_5Mg_8Cu_2Si_6$ intermetallics. With a strontium addition, dissolution of a large proportion of the needle-like $\beta$-$Al_5FeSi$ intermetallic in the aluminum matrix takes place; no transformation of this phase into any other intermetallics (including the $Al_{15}(Fe,Mn)_3Si_2$ phase) is observed. When both Mg and Sr are added, the diminution of the $\beta$-$Al_5FeSi$ phase is enhanced, through both its dissolution in the aluminum matrix as well as its transformation into $Al_8Mg_3FeSi_6$. The reactions and phases obtained have been analyzed using thermal analysis, optical microscopy, image analysis, and electron microprobe analysis (EMPA) coupled with energy-dispersive X-ray (EDX) analysis.

## I. INTRODUCTION

THE fact that they possess the essential characteristics of good castability, corrosion resistance, and machinability makes Al-Si foundry alloys excellent candidates for automotive applications. The silicon content in these alloys varies from 5 to 20 pct, with the eutectic occurring around 12 pct Si. Prominent among such alloys is the 319 alloy, with a silicon content of 6.0 to 6.5 pct, copper (Cu) in the amount of 3.5 pct, and magnesium (Mg) often being added for strengthening purposes.

The mechanical properties are controlled by the cast structure, *i.e.*, by the microstructural constituents that precipitate upon solidification, depending upon the composition and solidification conditions of the alloy.[1] These include, in addition to the $\alpha$-aluminum dendrites, the main Al-Si eutectic (where the eutectic Si particles are generally present as brittle, acicular platelets in the as-cast, nonmodified condition), Fe intermetallics (commonly, the $\alpha$-$Al_{15}(Fe,Mn)_3Si_2$ and $\beta$-$Al_5FeSi$ phases), secondary eutectic phases such as $Mg_2Si$ and $Al_2Cu$, and other complex intermetallics that result from the remaining liquid during the last stages of solidification.[2,3]

To enhance the alloy properties, modification of the eutectic silicon is usually carried out using strontium (Sr), to convert the silicon morphology from an acicular to a fibrous form. Among the intermetallics appearing in 319-type alloys, the $\beta$-$Al_5FeSi$ platelet/needlelike iron intermetallic is considered the most critical, as it significantly reduces the alloy ductility and fracture toughness, and different measures are adopted to *neutralize* its harmful effect.[4] In comparison, the $\alpha$-iron $Al_{15}(Fe,Mn)_3Si_2$ phase, due to its compact morphology (Chinese script–like in appearance), is less harmful to the mechanical properties. However, a coarser variation of the $\alpha$ phase, termed *sludge*, can also appear, in the form of polyhedral or *starlike* shaped particles,[5] where their hard, brittle nature can cause machining problems and tool wear.

The addition of Sr to the 1*XXX* and 6*XXX* series of wrought aluminum alloys has been reported to transform a major proportion of the $\beta$-$Al_5FeSi$ phase occurring in the ingots into the $\alpha$-$Al_8Fe_2Si$ scriptlike phase.[6,7] The Sr adsorbs to the latter and prevents the diffusion of silicon (which builds up at the Al matrix/$\alpha$-AlFeSi interface) into the $\alpha$-$Al_8Fe_2Si$ phase, resulting in an absence of $\beta$-$Al_5FeSi$ needles in the microstructure.[7] The present authors have observed, however, that rather than being *adsorbed*, the strontium is *absorbed* by the $\alpha$-$Al_8Fe_2Si$ phase, leading to its refinement and to ultrafine dendrite spacings on the order of 0.1 $\mu$m, compared to spacings of about 3.5 $\mu$m in the nonmodified alloy.[8]

Apparently, during solidification, the Sr addition leads to local segregation of iron in certain areas, such that the Fe/Si ratio is $>1$, which favors precipitation of iron intermetallics in the form of the compacted $\alpha$-$Al_8Fe_2Si$ phase.[9] A similar effect of Sr on Cu segregation in the 319 alloy, leading to

F.H. SAMUEL, Professor, and A.M. SAMUEL, Research Associate, are with the Department of Applied Sciences, University of Quebec at Chicoutimi, Chicoutimi PQ, Canada G7H 2B1. P. OUELLET, formerly Graduate Student, Department of Applied Sciences, University of Quebec at Chicoutimi, is Engineer with Montupet Ltée, Rivière-Beaudette, PQ, Canada J0P 1R0. H.W. DOTY, Materials Engineer, is with General Motors Corporation, GM Powertrain/MCT, Milford, NH 03055.

Manuscript submitted April 28, 1997.

**Table I. Chemical Compositions of the As-Received 319 Alloys**

| Alloy | Alloy Code | Element (Wt Pct) | | | | | | | | |
|---|---|---|---|---|---|---|---|---|---|---|
| | | Si | Fe | Cu | Mg | Mn | Ti | Cr | Sr | SF |
| A319.2 | G | 6.23 | 0.46 | 3.8 | 0.06 | 0.14 | 0.07 | 0.007 | <0.0001 | 0.76 |
| A319.1 | W | 5.85 | 0.79 | 3.2 | 0.09 | 0.34 | 0.14 | 0.08 | <0.0001 | 1.8 |

**Table II. Concentrations of Fe, Mn, Mg, and Sr Obtained from Chemical Analysis of the Melts Corresponding to Different Castings**

| Alloy Code | Element (Wt Pct) | | | |
|---|---|---|---|---|
| | Fe | Mn | Mg | Sr |
| G | 0.441 | 0.108 | 0.075 | — |
| GM2 | 0.377 | 0.097 | 0.600 | — |
| GS7 | 0.410 | 0.100 | 0.100 | 0.040 |
| GMST | 0.370 | 0.095 | 0.550 | 0.030 |
| W | 0.835 | 0.370 | 0.080 | — |
| WM5 | 0.770 | 0.334 | 0.512 | — |
| WS7 | 0.750 | 0.280 | 0.102 | 0.053 |
| WMS7 | 0.890 | 0.313 | 0.420 | 0.058 |

**Table III. Important Reactions Expected to Occur in A319.1 and A357 Alloys[2] (with Compositions Similar to Alloys Used in the Present Work)**

| Alloy | Reactions |
|---|---|
| A319.1 | $L \rightarrow Al_{15}(Fe,Mn,Cr)_3Si_2$ (sludge) |
| | $L \rightarrow \alpha$-Al dendritic network |
| | $L \rightarrow Al + Al_{15}(Fe,Mn)_3Si_2$ ($\alpha$-Chinese script phase) |
| | $L \rightarrow Al + Al_{15}(Fe,Mn)_3Si_2 + Al_5FeSi$* ($\beta$ needlelike phase) |
| | $L \rightarrow Al + Si + Al_5FeSi$ |
| | $L \rightarrow Al + Al_2Cu + Al_5FeSi + Si$ |
| | $L \rightarrow Al + Si + Al_2Cu + Al_5Mg_8Cu_2Si_6$ |
| A357 | $L \rightarrow Al$ |
| | $L \rightarrow Al + Si$ |
| | $L \rightarrow Al + Si + Al_5FeSi$ |
| | $L \rightarrow Al_5FeSi \rightarrow Al + Si + Al_8Mg_8FeSi_6$ |
| | $L \rightarrow Al + Si + Mg_2Si$ |
| | $L \rightarrow Al + Si + Mg_2Si + Al_8FeSi + Al_8Mg_3FeSi_6$ |

*High Fe content increases the range of existence of the $Al_5FeSi$ phase.

the formation of the blocklike $Al_2Cu$ intermetallic phase (containing about 40 pct Cu) rather than the finer (Al + $Al_2Cu$) eutectic (containing about 28 pct Cu) during solidification, has been reported.[3]

In Al-Si based alloys, while strontium is commonly added as a modifying agent, magnesium, often added to improve the alloy strength *via* $Mg_2Si$ precipitation following heat treatment, is also known to refine the silicon eutectic. While Sr modification of these alloys is well documented,[11] the effects of magnesium in this respect are not. The few studies found in the literature report Mg as having either a modifying or a coarsening effect on the eutectic silicon.[12,13]

As part of an ongoing program covering the development and properties of 319-type alloys in relation to automotive applications, where the effects of Mg and Sr have been studied in different contexts,[10,14,15] the present study was undertaken to investigate the individual and combined roles of Mg and Sr on the morphologies of Si, $Mg_2Si$, and the iron and copper intermetallics likely to form during the solidification of the 319-type alloy at very slow cooling rates. Two commercial 319-type alloys were used: a primary A319.2 alloy containing 0.46 wt pct Fe (coded G) and a secondary A319.1 alloy containing 0.79 wt pct Fe (coded W), respectively, in order to include the effects of Fe, Mn, and Cr contents with respect to the type of intermetallics formed. The reactions and phases obtained have been analyzed using thermal analysis, optical microscopy, image analysis, and electron microprobe analysis (EMPA) coupled with energy-dispersive X-ray (EDX) analysis and wavelength dispersion spectroscopy (WDS).

## II. EXPERIMENTAL

The chemical compositions and designated codes of the two 319-type alloys that were used are shown in Table I. The as-received alloys were supplied in the form of 12.5-kg ingots. The ingots were cut into smaller pieces, cleaned, dried, and melted in a 1-kg-capacity SiC crucible heated by means of an electric resistance furnace. The melting temperature was kept at 750 °C ± 5 °C. Measured quantities of Sr or Mg additions were made at this temperature, using a perforated graphite bell. Strontium was added in the form of an Al-10 wt pct Sr master alloy, while magnesium was added as pure metal. The melt was stirred for 15 minutes to ensure homogeneous mixing of the added material.

The molten metal was then poured into a cylindrical graphite mold (inner dimensions: 10-cm length, 6-cm diameter) preheated at 600 °C, to obtain close-to-equilibrium cooling conditions. Thermal analysis was performed for each casting by attaching a high-sensitivity thermocouple (chromel-alumel, type K) to the mold system, passing it through the bottom of the mold, and extending it halfway up into the mold cavity, along the mold centerline. The temperature-time data were recorded using a high-speed data acquisition system (acquisition speed of 0.2 seconds) linked to a computer. The part of the thermocouple within the mold was protected using double-walled ceramic tubing.

Several castings were made using G and W alloy melts containing various additions of Sr and Mg, and the corresponding cooling curves were recorded. Samplings for chemical analysis were also taken simultaneously for each pouring/casting. The results are shown in Table II. From the thermal analysis data, the cooling curves and their first derivatives were plotted in each case. The temperatures of formation of the Si eutectic and other precipitating phases were determined from the first derivative curves. The results are summarized in Tables III and IV for the two alloys, respectively.

Samples for metallographic examination (2.5 × 2.5 cm) were sectioned from each casting, from the central part of the casting containing the thermocouple tip, then mounted and polished for microstructural examination using an optical microscope (Olympus PMG3). A LECO* 2001 image analyzer was used in conjunction with the optical microscope for phase quantification purposes, wherever necessary.

*LECO is a trademark of the LECO Corporation, St. Joseph, MI.

**Table IV. Main Reactions Observed from the Thermal Analysis Diagrams of the A319.2 (G) Alloys Used in the Present Work**

| Alloy Code | Reaction Number | Temperature (°C) | Type of Reaction |
|---|---|---|---|
| G | 1 | 611.8 | formation of $\alpha$-Al dendritic network |
| | 2 | 600.0 to 572.7 | precipitation of pre-eutectic iron intermetallics ($\alpha$-$Al_{15}(Fe,Mn)_3Si_2$ and $\beta$-$Al_5FeSi$) |
| | 3 | 561.8 | precipitation of eutectic Si |
| | 4 | 550.0 to 541.0 | precipitation of posteutectic $\beta$-$Al_5FeSi$ |
| | 5 | 510.0 | precipitation of $Al_2Cu$ |
| | 6 | 502.7 | precipitation of $Al_5Mg_8Cu_2Si_6$ |
| GM2 | 1 | 608.2 | formation of $\alpha$-Al dendritic network |
| | 2 | 590.0 | precipitation of pre-eutectic iron intermetallics |
| | 3 | 546.3 | precipitation of eutectic Si |
| | 4 | 526.3 | transformation of $\beta$-$Al_5FeSi$ into $Al_8Mg_3FeSi_6$ |
| | 5 | 521.8 | precipitation of $Mg_2Si$ |
| | 6 | 501.8 | precipitation of $Al_2Cu$ |
| | 7 | 491.8 | precipitation of $Al_5Mg_8Cu_2Si_6$ |
| GS7 | 1 | 609.1 | formation of $\alpha$-Al dendritic network |
| | 2 | 595.4 | precipitation of pre-eutectic iron intermetallics |
| | 3 | 553.6 | precipitation of eutectic Si |
| | 4 | 535.4 | precipitation of $\beta$-$Al_5FeSi$ |
| | 5 | 511.8 | precipitation of $Al_2Cu$ |
| | 6 | 504.5 | precipitation of $Al_5Mg_8Cu_2Si_6$ |
| GMST | 1 | 608.2 | formation of $\alpha$-Al dendritic network |
| | 2 | 597.2 | precipitation of pre-eutectic $\beta$-$Al_5FeSi$ |
| | 3 | 550.0 | precipitation of eutectic Si |
| | 4 | 531.8 | (a) precipitation of posteutectic $\beta$-$Al_5FeSi$<br>(b) transformation of $\beta$-$Al_5FeSi$ into $Al_8Mg_3FeSi_6$ |
| | 5 | 522.8 | precipitation of $Mg_2Si$ |
| | 6 | 502.7 | precipitation of $Al_2Cu$ |
| | 7 | 491.8 | precipitation of $Al_5Mg_8Cu_2Si_6$ |

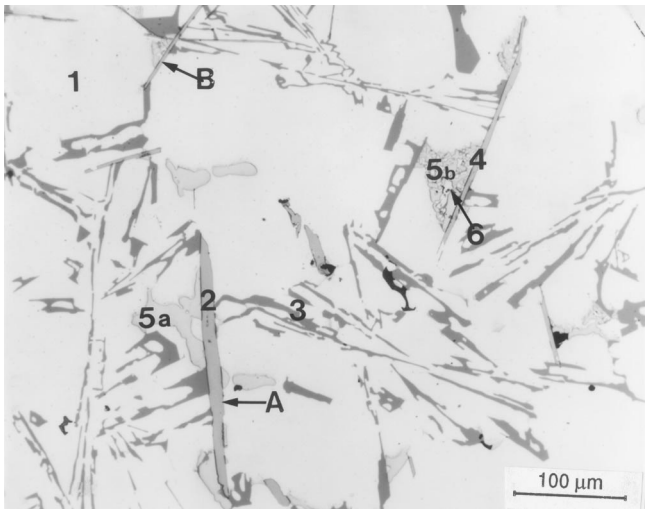


Fig. 1—Microstructure of as-solidified A319.2 (G) alloy showing (1) $\alpha$-Al dendrite, (2) pre-eutectic $\beta$-$Al_5FeSi$, (3) eutectic Si, (4) posteutectic $\beta$-$Al_5FeSi$, (5a) blocklike $Al_2Cu$, (5b) eutectic Al + $Al_2Cu$, and (6) $Al_5Mg_8Cu_2Si_6$ phase particles.

For the $\beta$-needle measurements, the number of fields examined for each sample (the term *field* representing the field of view of the optical microscope, covering an area of $2.2608 \times 10^4$ $\mu m^2$ at 500 times magnification) was chosen so as to cover the entire area of the sample, the sample surface being traversed in a regular, systematic fashion and the $\beta$-needle characteristics noted for the selected number of fields.

The various phases reported in this study were identified using EMPA coupled with EDX analysis and WDS, employing a Noran Instruments microanalyzer operating at 15 kV and 20nA, using an electron beam with a diameter of about 5 $\mu$m. In each case, at least 5 to 6 measurements were taken (using a point count of 20 seconds for each reading) to obtain the average composition.

## III. RESULTS AND DISCUSSION

Backerud *et al.*[2] have studied the reactions that can occur during solidification for a wide range of foundry aluminum alloys. Those corresponding to the A319 and A357 alloys (similar in composition to the 319-type and Mg-containing 319-type alloys used in the present work) are listed in Table III.

To facilitate an understanding of the phases that will be mentioned in connection with the reactions that were observed for different cooling curves (described in Section III–A), the microstructure typically obtained from the A319.2 (G) base alloy is shown in Figure 1. The various phases that precipitate (marked 1 through 6 in the figure) can be clearly seen, and are identified as follows:

(1) an $\alpha$-Al dendrite;
(2) a pre-eutectic $\beta$-$Al_5FeSi$ particle (needle shaped);
(3) an eutectic Si particle;
(4) a posteutectic $\beta$-$Al_5FeSi$ particle (needle shaped);
(5a) a blocklike $Al_2Cu$ phase particle;
(5b) an eutectic (Al + $Al_2Cu$) phase particle; and
(6) an $Al_5Mg_8Cu_2Si_6$ phase particle.

This micrograph will be referred to again, when the microstructural aspects are further discussed, in Section III–B.

**Table V. Main Reactions Observed from the Thermal Analysis Diagrams of the A319.1 (W) Alloys Used in the Present Work**

| Alloy Code | Reaction Number | Temperature (°C) | Type of Reaction |
|---|---|---|---|
| W | 1 | 607.3 | formation of $\alpha$-Al dendritic network |
| | 2 | 594.1 | precipitation of $\alpha$-$Al_{15}(Fe,Mn)_3Si_2$ |
| | 3 | 572.7 | precipitation of pre-eutectic $\beta$-$Al_5FeSi$ |
| | 4 | 561.8 | precipitation of eutectic Si |
| | 5 | 550.0 | precipitation of posteutectic $\beta$-$Al_5FeSi$ |
| | 6 | 538.2 | precipitation of $Mg_2Si$ |
| | 7 | 505.5 | precipitation of $Al_2Cu$ |
| WM5 | 1 | 605.5 | formation of $\alpha$-Al dendritic network |
| | 2 | 589.1 | precipitation of $\alpha$-$Al_{15}(Fe,Mn)_3Si_2$ |
| | 3 | 572.7 | precipitation of pre-eutectic $\beta$-$Al_5FeSi$ |
| | 4 | 553.7 | precipitation of eutectic Si |
| | 5 | 532.9 | transformation of $\beta$-$Al_5FeSi$ into $Al_8Mg_3FeSi_6$ |
| | 6 | 521.7 | precipitation of $Mg_2Si$ |
| | 7 | 495.4 | (a) precipitation of $Al_2Cu$<br>(b) precipitation of $Al_5Mg_8Cu_2Si_6$ |
| WS7 | 1 | 610.0 | formation of $\alpha$-Al dendritic network |
| | 2 | 580.0 | precipitation of $\alpha$-$Al_{15}(Fe,Mn)_3Si_2$ |
| | 3 | 568.2 | precipitation of pre-eutectic $\beta$-$Al_5FeSi$ |
| | 4 | 550.0 | precipitation of eutectic Si |
| | 5 | 527.3 | precipitation of posteutectic $\beta$-$Al_5FeSi$ |
| | 6 | 505.4 | precipitation of $Al_2Cu$ |
| WMS7 | 1 | 605.5 | formation of $\alpha$-Al dendritic network |
| | 2 | 579.1 | endothermic reaction—dissolution of $\beta$-$Al_5FeSi$ |
| | 3 | 553.6 | precipitation of eutectic Si |
| | 4 | 528.2 | (a) precipitation of posteutectic $\beta$-$Al_5FeSi$<br>(b) transformation of $\beta$-$Al_5FeSi$ into $Al_8Mg_3FeSi_6$ |
| | 5 | 521.8 | precipitation of $Mg_2Si$ |
| | 6 | 498.1 | precipitation of $Al_2Cu$ |
| | 7 | 488.1 | precipitation of $Al_5Mg_8Cu_2Si_6$ |

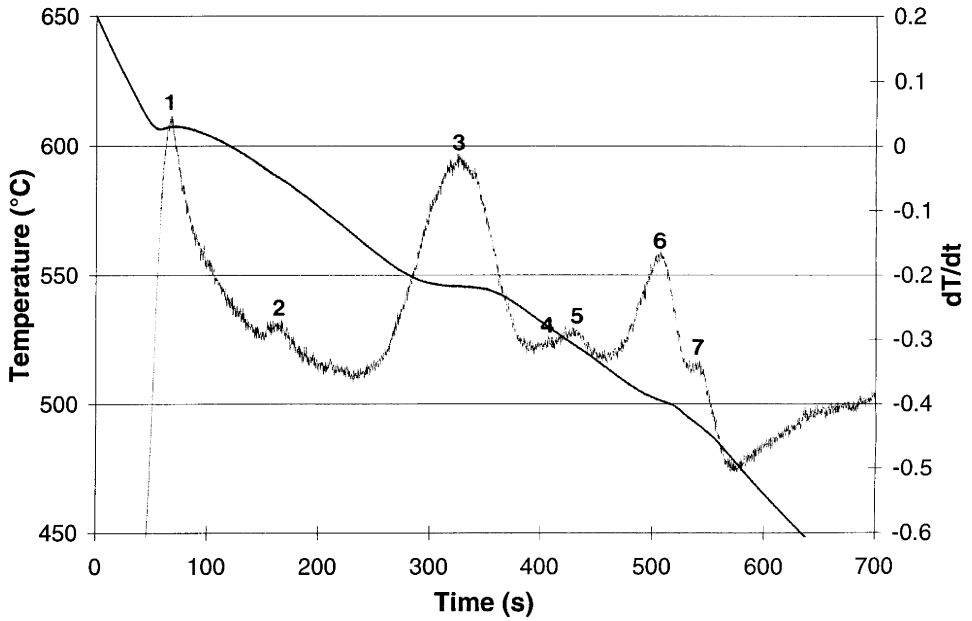


Fig. 2—Temperature-time cooling curve and its first derivative obtained from GM2 alloy (A319.2 + 0.6 wt pct Mg).

A. *Cooling Curves*

As mentioned previously, thermal analysis was carried out for the various alloy melt castings that were poured. From the corresponding temperature-time cooling curves, the first derivatives were obtained, and the resulting peaks were identified. Tables IV and V summarize, respectively, the main reactions and the temperatures at which they occurred for the two 319-type alloys (the primary A319.2 alloy, coded G, and the secondary A319.1 alloy, coded W), with different Mg and/or Sr additions. A representative example of the type of cooling curve that was obtained is shown in Figure 2, for the case of an A319.2 alloy casting containing 0.52 wt pct Mg (coded GM2), where the numbers 1 through 7 marked on the first derivative curve refer to the corresponding reactions described in Table IV for GM2 alloy.

**Table VI. Comparison of Reactions Occurring in A319.2 Alloy Containing 0.06 Wt Pct and 1.2 Wt Pct Mg**

| 0.06 Wt Pct Mg (Alloy Code G) | | 1.2 Wt Pct Mg (Alloy Code GM10) | |
|---|---|---|---|
| 1 | formation of $\alpha$-Al dendritic network | 1 | formation of $\alpha$-Al dendritic network |
| 2 | precipitation of pre-eutectic $\beta$-$Al_5FeSi$ phase | 2 | precipitation of eutectic Si phase |
| 3 | precipitation of eutectic Si phase | 3 | transformation of $\beta$-$Al_5FeSi$ into $Al_8Mg_3FeSi_6$ |
| 4 | precipitation of posteutectic $\beta$-$Al_5FeSi$ phase | 4 | precipitation of $Mg_2Si$ phase |
| 5a | precipitation of blocky $Al_2Cu$ phase | 5 | precipitation of $Al_2Cu$ phase |
| 5b | precipitation of eutectic (Al + $Al_2Cu$) phase | | |
| 6 | precipitation of $Al_5Mg_8Cu_2Si_6$ phase | 6 | precipitation of $Al_5Mg_3Cu_2Si_6$ phase |

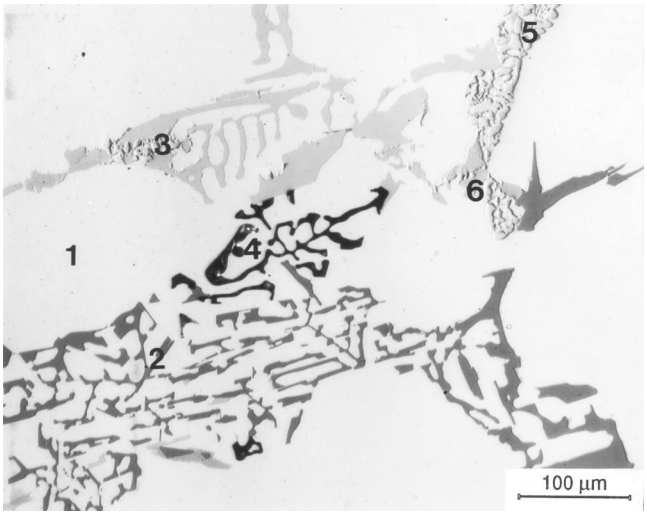


Fig. 3—Microstructure of as-solidified GM10 alloy (A319.2 + 1.2 wt pct Mg) showing (1) $\alpha$-Al dendrite, (2) eutectic Si, (3) $Al_8Mg_3FeSi_6$, (4) $Mg_2Si$, (5) $Al_2Cu$, and (6) $Al_5Mg_8Cu_2Si_6$ phase particles.

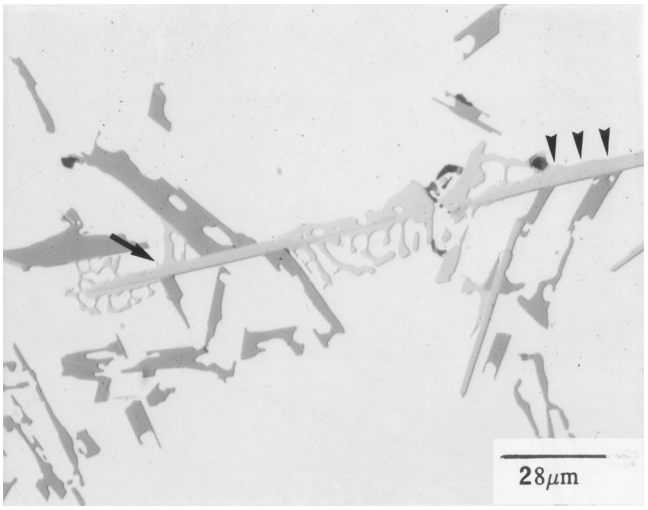


Fig. 4—Microstructure of a synthetic Al-6.5 wt pct Si alloy containing 0.6 wt pct Fe and 0.53 wt pct Mg showing transformation of the $\beta$-$Al_5FeSi$ phase into $Al_8Mg_3FeSi_6$. Note the uneven edge of the $\beta$-$Al_5FeSi$ needle along the side where the transformation is expected to take place (short arrows).

In the A319.2-based alloy, a shallow peak extending over a wide temperature range (~600 °C to 573 °C) is normally observed, representing the pre-eutectic precipitation of iron intermetallics in the mushy (liquid/solid) zone during the progress of solidification. With the addition of Mg, Sr, or Mg + Sr, however, a distinct peak develops, as shown by peak 2 in Figure 2. Another important feature associated with an increased Mg concentration is the precipitation of the $Al_5Mg_8Cu_2Si_6$ phase, indicated clearly by peak 7, that follows $Al_2Cu$ precipitation (peak 6). The peak corresponding to the $Mg_2Si$ phase is always found to occur diffused together with that occurring due to the transformation of the $\beta$-$Al_5FeSi$ phase into the $Al_8Mg_5FeSi_6$ phase (peak 4, Figure 2).

Although the other cooling curves are not shown, modification with strontium (400 ppm Sr addition, GS7 alloy casting) was seen to significantly reduce the peak corresponding to the pre-eutectic $\beta$-$Al_5FeSi$ phase precipitation, indicating the progress of dissolution of the latter, confirming our earlier investigations about the effect of Sr on this particular intermetallic.[10] The effect of Sr on the other reactions, however, was minimal.

The cooling curves also revealed that the depression in the Si eutectic temperature was more pronounced with the Mg addition than with Sr (Table IV) and that a combined Mg + Sr addition produced shallow peaks (refer to the GMST alloy casting, Table IV), whose intensities lay halfway between those observed for the Mg- or Sr-modified alloys.

In the case of the secondary A319.1 alloy, the base alloy (W) showed two peaks caused by the precipitation of the iron intermetallics (Table V), followed by the peak for the eutectic silicon, followed by a large shallow peak covering the posteutectic $\beta$-$Al_5FeSi$ phase precipitation. Precipitation of the $Al_5Mg_8Cu_2Si_6$ phase, however, was not observed. One must bear in mind that the secondary alloy contains a much higher iron content (about 0.8 to 0.9 wt pct), so that, with an Mn content of 0.34 wt pct, the Fe/Mn ratio is close to 2:1—a ratio that favors precipitation of the Chinese script–like $\alpha$-$Al_{15}(Fe,Mn)_3Si_2$ iron intermetallic phase before that of the pre-eutectic $\beta$-$Al_5FeSi$.

The addition of 0.5 wt pct Mg did not produce noticeable reactions in the liquid/solid zone. Immediately after precipitation of the eutectic silicon, however, two distinct peaks were clearly seen, corresponding to the transformation of the $\beta$-$Al_5FeSi$ phase into $Al_8Mg_3FeSi_6$ and precipitation of the $Mg_2Si$ phase, respectively.

Modification with Sr resulted in lowering the precipitation temperature of the $\alpha$-$Al_{15}(Fe,Mn)_3Si_2$ phase, without noticeably changing that of the $\beta$-$Al_5FeSi$ phase. While posteutectic precipitation of the latter was also observed, no peak corresponding to $Mg_2Si$ precipitation was found. Simultaneous additions of Mg and Sr resulted in a ''negative'' peak in the liquid/solid zone (refer to the WMS7 alloy, Table V); other reactions were similar to those observed for the primary alloy with an Mg + Sr addition (GMS alloy, Table IV).

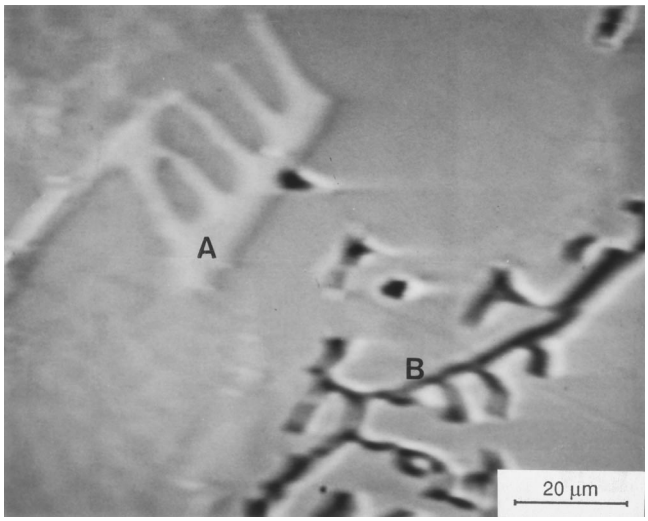


(*a*)


(*b*)

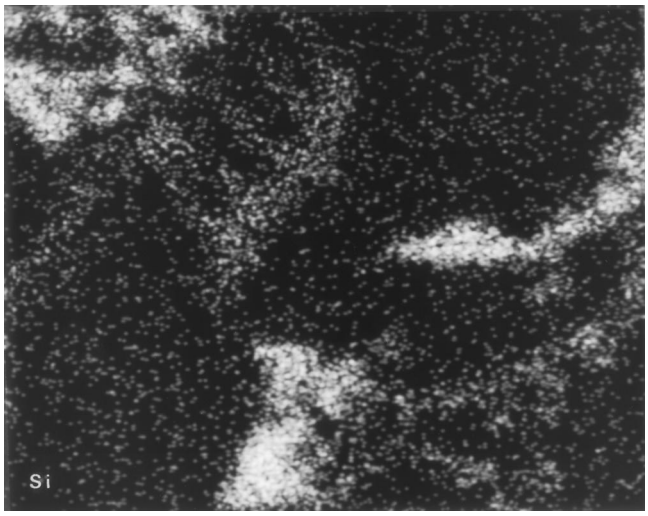


(*c*)

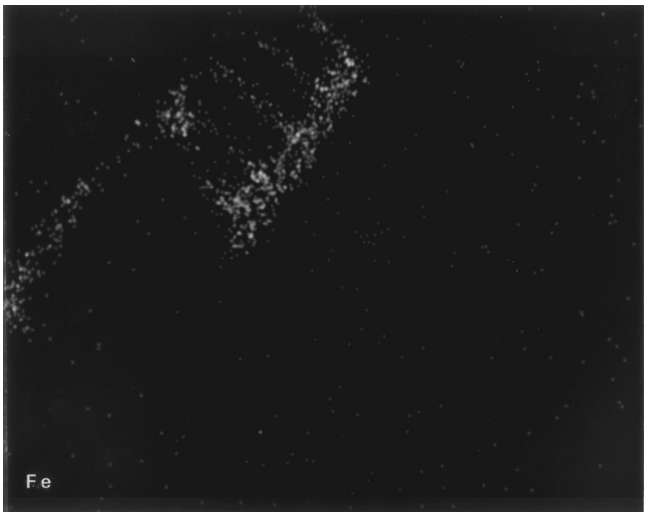


(*d*)

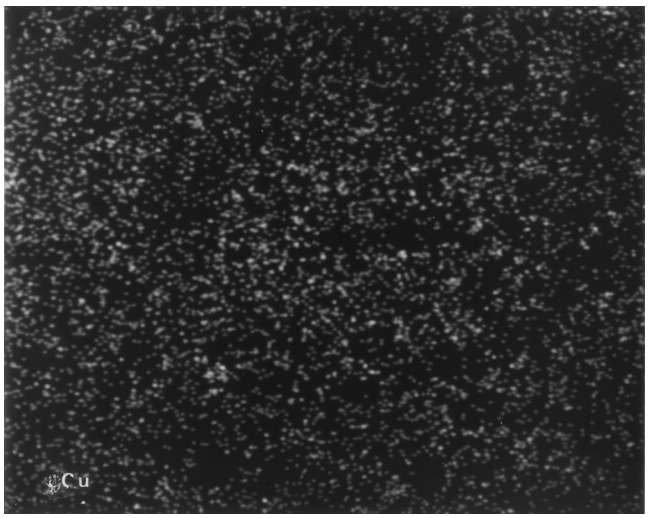


(*e*)

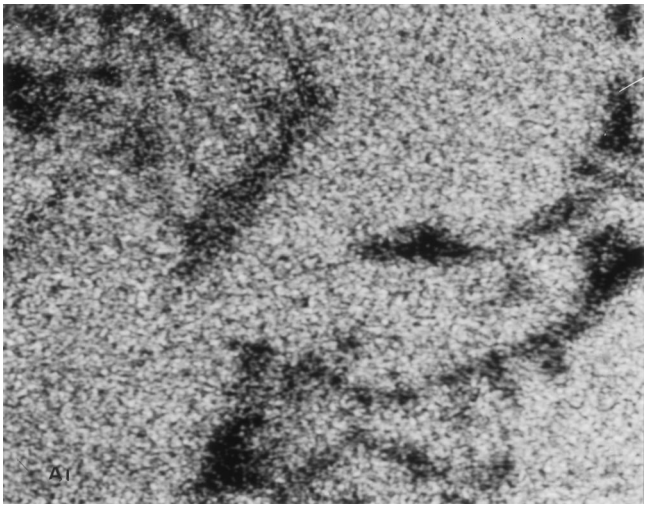


(*f*)

Fig. 5—(*a*) Backscattered electron image of and X-ray images showing distribution of (*b*) Mg, (*c*) Si, (*d*) Fe, (*e*) Cu, and (*f*) Al in the $Al_8Mg_3FeSi_6$ (marked A) and $Mg_2Si$ (marked B) phase particles observed in the GM10 alloy (A319.2 + 1.2 wt pct Mg).

B. *Microstructural Observations and Phase Identification*

1. *Precipitation of iron intermetallics*

The microstructure of the A319.2 (G) alloy shown in Figure 1 comprises two distinct types of $\beta$-$Al_5FeSi$ needles/platelets: pre-eutectic particles (marked A), characterized by their large size, and co- or posteutectic particles (marked B), which are relatively thin. The difference in their size is directly related to the rates of diffusion of the iron atoms with respect to the temperatures at which the two particle types precipitate.

In order to arrive at a clear understanding of the role of magnesium with respect to the precipitation of these intermetallics, the Mg content of the A319.2 alloy was increased to ~1.2 wt pct (coded as alloy GM10). The microstructure of the metallographic sample obtained from the corresponding casting (Figure 3) shows that the $\beta$-$Al_5FeSi$ needles are completely replaced by the $Al_8Mg_3FeSi_6$ phase (pale gray color and dendritic Chinese script–like morphology, marked as 3). Also to be noted in Figure 3 is the precipitation of the $Mg_2Si$ phase, in script form (black, marked 4). For comparison purposes, the reactions that occur during solidification of the A319.2 alloy containing 0.06 wt pct Mg (base alloy G) or 1.2 wt pct Mg (alloy GM10) are listed in Table VI, and the phases are identified by their corresponding numbers in Figures 1 and 3, respectively.

The transformation of the $\beta$-$Al_5FeSi$ phase into the $Al_8Mg_3FeSi_6$ phase is best illustrated by Figure 4, depicting the microstructure of a synthetic Al-6.5 pct Si alloy containing 0.6 wt pct Fe and 0.53 wt pct Mg. As the transformation is a posteutectic reaction, the transformed phase is seen to occur in places where no other phase (*i.e.*, eutectic Si) is already present (refer to the arrow on the left-hand side, as well as the central area in the micrograph). The short arrows to the right highlight the uneven edge of the $\beta$-$Al_5FeSi$ needle prior to its transformation, as compared to its straight edge on the opposite side and elsewhere in areas occupied by the Si particles.

An EMPA was used to determine the composition of the new intermetallic phase ($Al_8Mg_3FeSi_6$) observed in Figure 3. The backscattered electron images of $Al_8Mg_3FeSi_6$ and $Mg_2Si$, displayed in Figure 5(a), show that both phases are having scriptlike morphologies, while the series of X-ray images given in Figures 5(b) through (f) reveal that the only elements associated with the former (marked A in Figure 5(a)) are Fe, Mg, Si, and Al. In Figure 5(a), since the atomic weight of iron is higher than that of Si (55.85 and 28.08, respectively), the iron-containing phase is lighter in color than the $Mg_2Si$ phase (marked B). As expected, the Mg intensity of the $Mg_2Si$ particle is noticeably higher than that of the $Al_8Mg_3Si_6$-phase particle, with both exhibiting more or less similar Si intensities (Figure 5(c)). The X-ray image of Fe distribution is displayed in Figure 5(d), where most of the iron is found to be concentrated in the $Al_8Mg_3FeSi_6$ particle. In contrast, copper and aluminum are found to be more densely distributed in the matrix, rather than in any of the two intermetallics, as seen from Figures 5(e) and (f), respectively.

An example of the EDX spectrum obtained from the new iron intermetallic, $Al_8Mg_3FeSi_6$, is shown in Figure 6, comprising reflections due to Mg, Si, Fe, and Al. The relative atomic concentrations listed in Table VII suggest a chemical composition corresponding to $Al_{11.7}Mg_{3.4}FeSi_6$, approximately close to $Al_8Mg_3FeSi_6$.[16] Obviously, the higher Al concentration observed has been somewhat affected by the aluminum from the surrounding matrix.

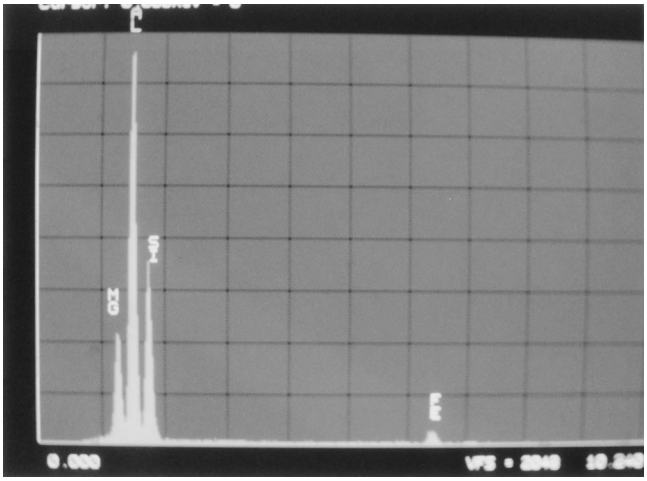

Fig. 6—EDX spectrum corresponding to the $Al_8Mg_3FeSi_6$ phase.

The microstructure of the A319.2 alloy modified with Sr (coded GS7) is presented in Figure 7(a), where only very few needles of the $\beta$-$Al_5FeSi$ phase are seen (arrowed). From the findings of Backerud *et al.*[2] that the pre-eutectic $\beta$ needles are characterized by their large size (both length and thickness), we may presume that these needles probably formed following the precipitation of eutectic silicon, *i.e.*, in a posteutectic reaction. This observation is in good agreement with our earlier findings on the effectiveness of Sr in dissolving $\beta$ needles, in particular, those that are formed in the pre-eutectic temperature range, *i.e.*, in the mushy-zone region.[10] In that study, it was observed that, from among the A319.2 alloy samples obtained from degassed, degassed + grain-refined, degassed + 300 ppm Sr-modified, and degassed + grain-refined + Sr-modified melts, the degassed + Sr-modified sample possessed the lowest $\beta$-needle density.

Similarly, Mg and Mg + Sr additions to the A319.2 alloy were also found to reduce the volume fraction (amount) of $\beta$ needles observed in the base alloy. As reported elsewhere,[17] the data obtained from $\beta$-needle measurements (carried out following the procedures described in Section II) were analyzed and tabulated in the form of $\beta$-needle count *vs* length-range values (in increasing increments of 20 $\mu$m), over the entire range of $\beta$-needle lengths observed in each case. The $\beta$-needle length distributions obtained for the base (G), base + Mg, and base + Mg + 300 ppm Sr alloy samples revealed that the number of $\beta$-phase particles was considerably reduced in the latter two cases (by more than two-thirds). In addition, the nature of the distributions (*i.e.*, a shift in the peaks toward the right) also indicated that the pre-eutectic $\beta$ needles had been dissolved or broken into smaller fragments.

From the present study, based on our observations of the transformation of the $\beta$-$Al_5FeSi$ phase into $Al_8Mg_3FeSi_6$, the reduction in the volume fraction of $\beta$ needles may also be attributed in part to such a transformation, in addition to their dissolution in the aluminum matrix. An example of the fragmentation of pre-eutectic $\beta$-$Al_5FeSi$ needles prior to their dissolution in a Sr-modified GS7 alloy is shown in Figure 7(b).

**Table VII. Elemental Analysis (Atomic Percent) of the Iron and Copper Intermetallics Shown in Various Figures**

| Figure Number | Element (At. Pct) | | | | | | | Suggested Composition |
|---|---|---|---|---|---|---|---|---|
| | Al | Si | Mg | Fe | Mn | Cr | Cu | |
| 5(a) | 54.33 | 25.04 | 15.99 | 4.65 | — | — | — | $Al_{11.7}Mg_{3.4}Si_{5.4}Fe$ |
| 10(a) | 72.33 | 10.27 | — | 10.06 | 5.01 | 2.32 | — | $Al_{14.1}(Fe,Mn,Cr)_{3.4}Si_2$ |
| 10(a) | 72.89 | 9.90 | — | 9.30 | 5.33 | 2.57 | — | $Al_{14.8}(Fe,Mn,Cr)_{3.5}Si_2$ |
| 10(a) | 71.30 | 11.16 | — | 10.20 | 5.02 | 2.32 | — | $Al_{12.8}(Fe,Mn,Cr)_{3.1}Si_2$ |
| 12(b) | 56.83 | 35.11 | 5.61 | — | — | — | 2.45 | out of stoichiometry |
| 17(a) | 64.19 | 1.8 | — | — | — | — | 34.02 | $Al_{1.8}Cu$ |
| 17(b) | 23.24 | 24.37 | 38.29 | — | — | — | 9.1 | $Al_{2.6}Mg_{4.2}Si_{2.7}Cu$ |

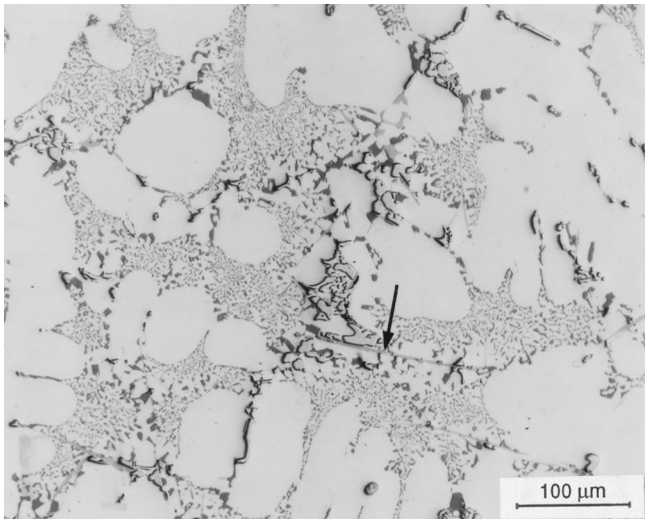


(*a*)

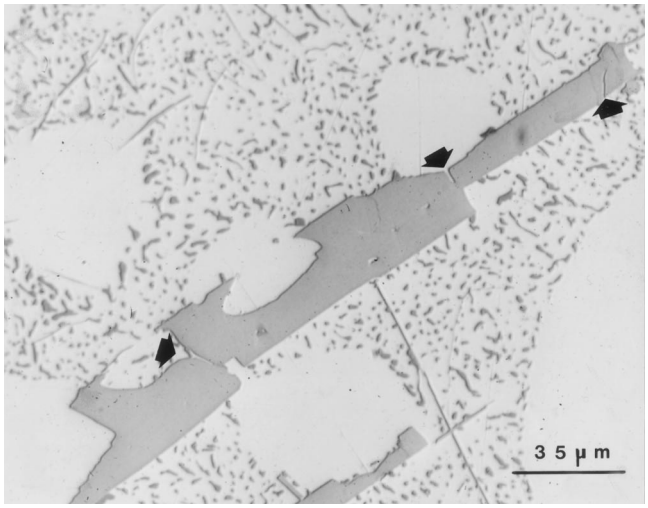


(*b*)

Fig. 7—Microstructure of Sr-modified A319.2 (GS7) alloy showing (*a*) dissolution of the $\beta$-$Al_5FeSi$ phase (arrow points to what is probably a posteutectic $\beta$ needle) and (*b*) fragmentation of a pre-eutectic $\beta$-needle.

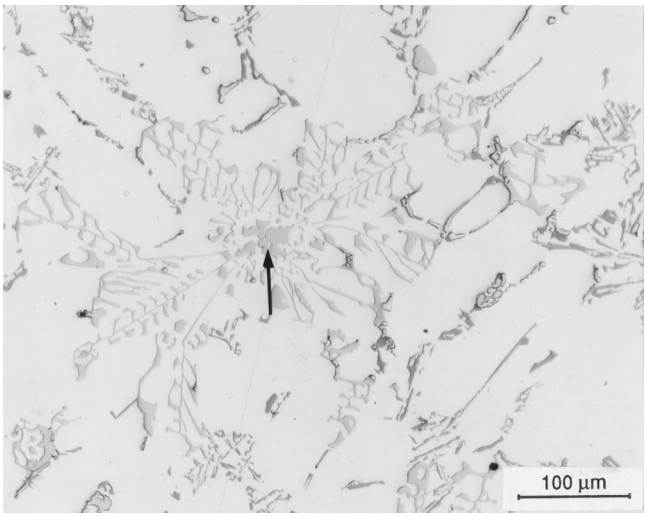


(*a*)

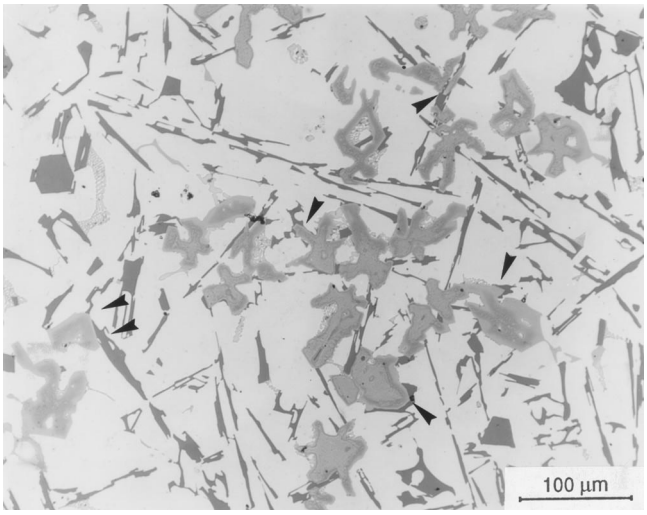


(*b*)

Fig. 8—Microstructure of A319.1 (W) alloy showing (*a*) change in morphology of a starlike phase particle (arrowed) into Chinese script during solidification and (*b*) segregation of the starlike phase particles.

In alloys that contain relatively higher amounts of Fe and Mn, typical of the secondary A319.1 (W) alloy, the first iron intermetallic expected to form is sludge, also described as the star-like phase, followed by the $\alpha$-$Al_{15}(Fe,Mn)_3Si_2$ Chinese script–like phase. As both intermetallics have the same chemical composition, *i.e.*, $Al_{15}(Fe,Mn,Cr)_3Si_2$, the two phases are commonly observed joined together, as shown in Figure 8(a). The arrow points to the presence of a starlike particle with several $\alpha$-Chinese script–like particles growing out of it in different directions. It is interesting to find that, when the starlike particles segregate in a certain area on account of their higher density compared to that of liquid aluminum, no other iron intermetallics are seen to form in the neighboring areas (Figure 8(b), arrows). It should be kept in mind that the star-like phase forms above

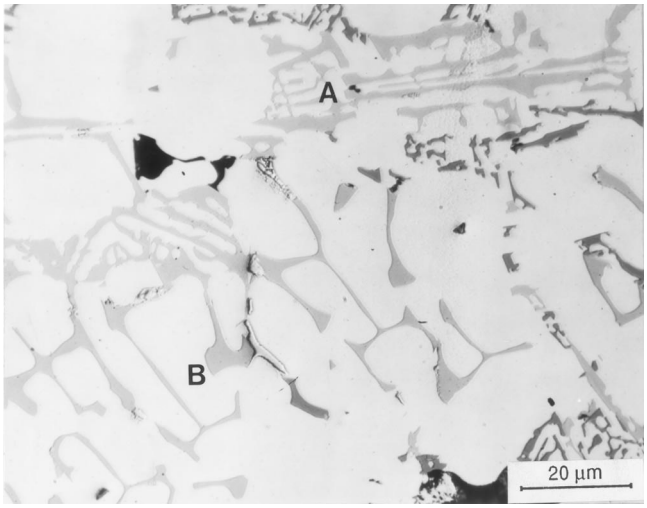


(*a*)

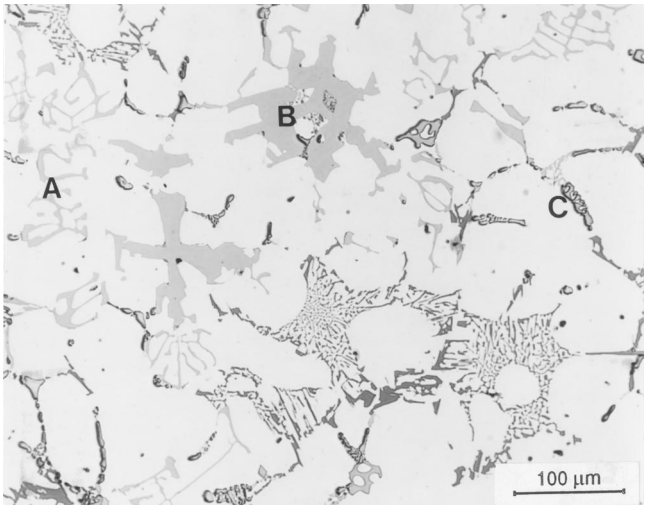


(*b*)

Fig. 9—Microstructure of WM5 alloy (A319.1 + 0.5 wt pct Mg) showing how the $Al_8Mg_3FeSi_6$ phase (marked A) has completely replaced the $\beta$-$Al_5FeSi$ needles (B marks the $\alpha$-$Al_{15}(Fe,Mn)_3Si_2$ phase) and (*b*) segregation of the $\alpha$-Chinese script (A), starlike (B), and $Al_2Cu$ (C) intermetallics ahead of the eutectic Si colonies.

the liquidus line, where the diffusion of iron atoms is fairly rapid.

Figure 9(a) shows how the addition of Mg, in amounts of 0.5 wt pct or more, to the molten A319.1 alloy results in transforming the remaining $\beta$-$Al_5FeSi$ needles into the $Al_8Mg_3FeSi_6$ Chinese script–like phase (marked A), without altering the morphology or the chemical composition of the other pre-eutectic iron intermetallics, *i.e.*, the $\alpha$-$Al_{15}(Fe,Mn)_3Si_2$ Chinese script–like phase (marked B), as was also confirmed by EDX analysis. Simultaneous additions of Mg and Sr to the A319.1 alloy (*i.e.*, the WMS7 alloy) leads to the complete disappearance of the $\beta$ needles, as shown in Figure 9(b). It is evident that Sr causes noticeable segregation of the $\alpha$-Chinese script–like, starlike, and $Al_2Cu$ intermetallics (marked A, B, and C, respectively, in Figure 9(b)) ahead of the advancing eutectic silicon colonies. The $\alpha$-Chinese script–like phase particles are seen to be rather dispersed, with sizes smaller than the large fanlike particles shown in Figure 8(a).

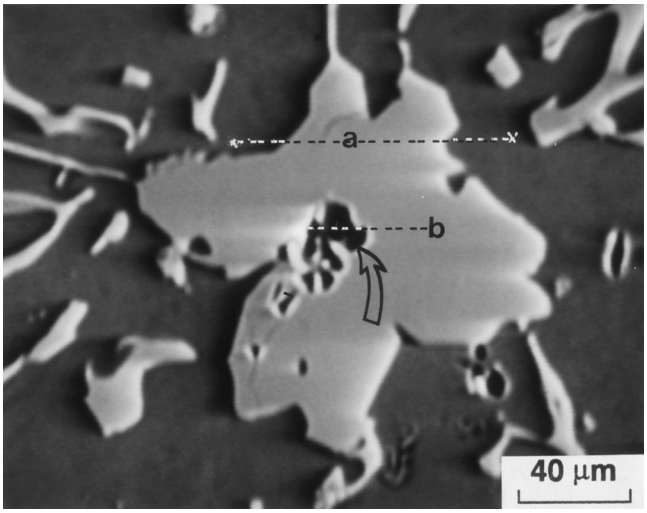


(*a*)

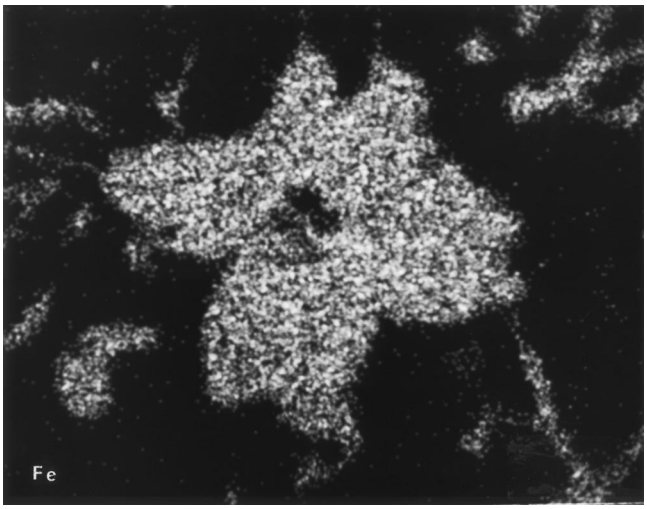


(*b*)

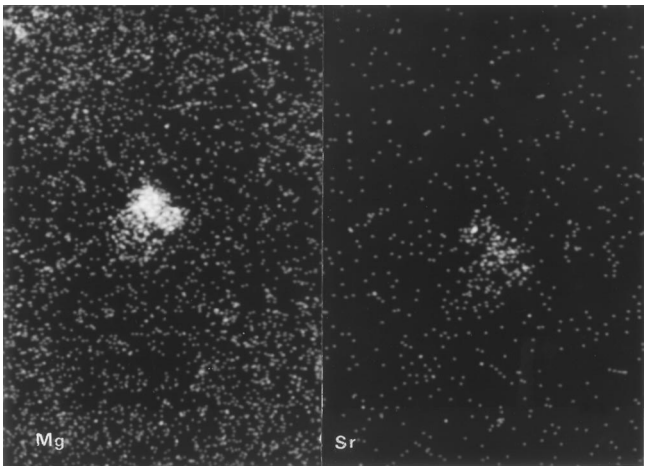


(*c*)

Fig. 10—(*a*) Backscattered image of and X-ray images showing (*b*) Fe and (*c*) Mg and Sr distributions in the starlike intermetallic phase observed in Sr-modified A319.1 alloy containing 0.42 wt pct Mg (WMS7 alloy).

An EMPA was used to determine the composition of the starlike phase shown in Figure 9(b). A series of backscattered and X-ray images of this phase is given in Figure 10.

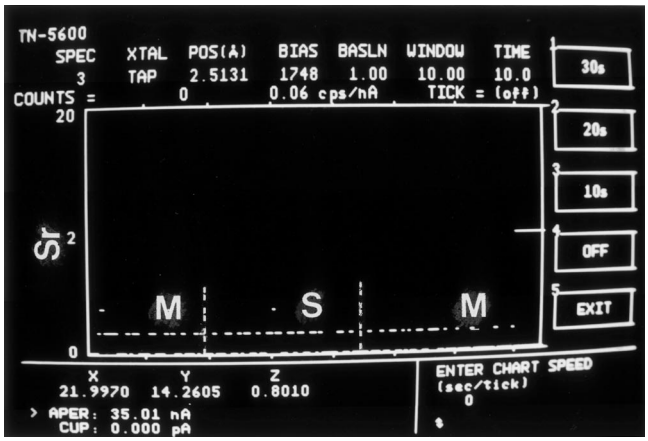


(*a*)

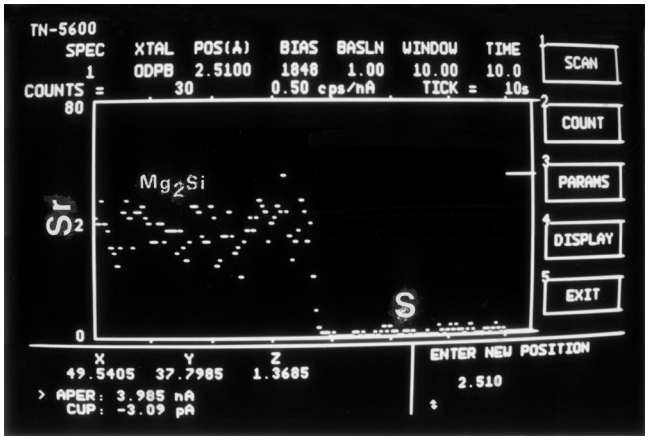


(*b*)

Fig. 11—Line scans taken across paths a and b shown in Fig. 10(a) showing the Sr concentration (*a*) across the Al matrix (M)–starlike particle (S)–Al matrix (M) of path a, and (*b*) in the $Mg_2Si$ particle situated in the center of the starlike particle ($Mg_2Si$) and the starlike particle itself (S), along path b.

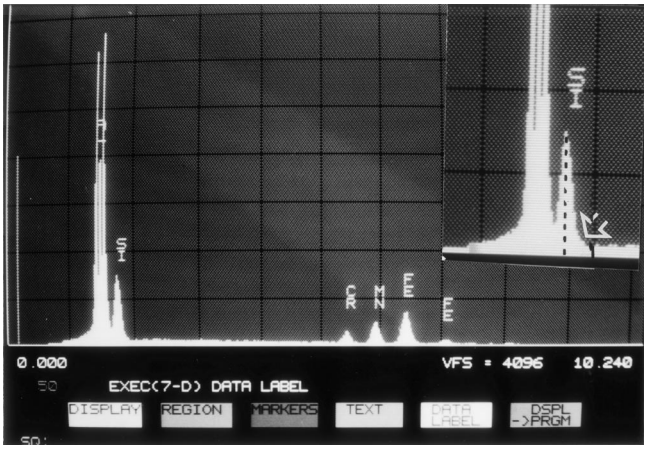


(*a*)

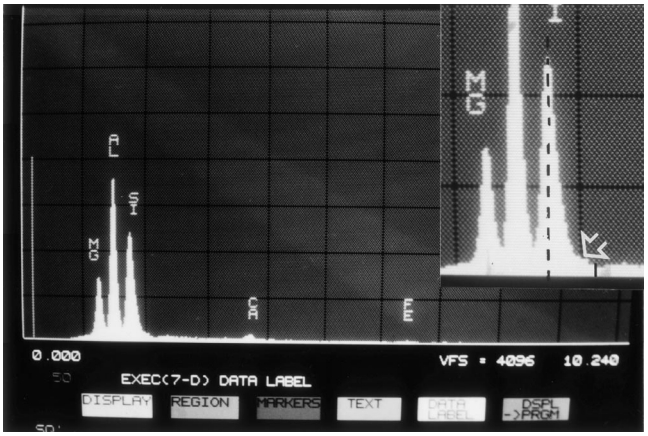


(*b*)

Fig. 12—EDX spectra corresponding to (*a*) $Al_{15}(Fe, Mn,Cr)_3 Si_2$ starlike intermetallic and (*b*) scriptlike $Mg_2Si$ particles.

The backscattered electron image, Figure 10(a), shows how the $\alpha$-Chinese script–like phase particles grow out of the starlike phase particle during solidification. It is interesting to note the presence of fragments of a black scriptlike $Mg_2Si$ particle at the center of the starlike particle (note the open arrow in Figure 10(a)). The X-ray images of Fe and the Mg and Sr distributions are shown in Figures 10(b) and (c), respectively. As both the starlike and $\alpha$-Chinese script–like phases have approximately the same chemical compositions, the iron appears to be distributed evenly in the two phases (Figure 10(b)), while the X-ray image of Mg is seen to be associated mainly with the $Mg_2Si$ particle (Figure 10(c)). The X-ray image of Sr, however, reveals that it is also densely concentrated in the $Mg_2Si$ particle, with a relatively negligible concentration elsewhere in the starlike particle (close to the zero-detection limit of the Noran instrument used in the present study).

These observations were confirmed by the line scans shown in Figure 11, which were taken along the paths marked a and b in Figure 10(a). Accordingly, the label M-S-M in Figure 11(a) implies the matrix–starlike phase–matrix line scan corresponding to path a, while $Mg_2Si$ and S in Figure 11(b) correspond to the line scan taken across the black $Mg_2Si$ scriptlike particle situated at the center of the starlike particle and into the latter, along path b. Thus, the main role of Sr lies in the fragmentation/modification of the $Mg_2Si$ phase, as suggested by Flood *et al.*,[18] and not in the nucleation of the starlike phase, as has been reported elsewhere.[19]

Figure 12(a) shows the EDX spectrum obtained from the starlike phase particle of Figure 10(a), where the only elements associated with it are found to be Fe, Mn, Cr, Si, and Al. Analysis of different parts of the particle showed that its chemical composition ranged between $Al_{12}(Fe,Mn,Cr)_3Si_2$ and $Al_{15}(Fe,Mn,Cr)_3Si_2$ (Table VII), which is in good agreement with the results published by Granger.[20] The EDX spectrum obtained from the $Mg_2Si$ particle is shown in Figure 12(b), and the relative atomic concentrations are listed in Table VII. On account of the small size of the $Mg_2Si$ particle, the Si concentration is much higher than what is expected at the stoichiometric concentration. The enlarged insets in Figure 12 clearly show that the Si peak for the $Mg_2Si$ particle is somewhat broader than that for the $Al_{15}(Fe,Mn,Cr)_3Si_2$ particle. This broadening may be accounted for by an overlapping of the Si and Sr peaks, with their respective $K_\alpha$ and $L_\alpha$ lines occurring at 1.76 and 1.806 keV.

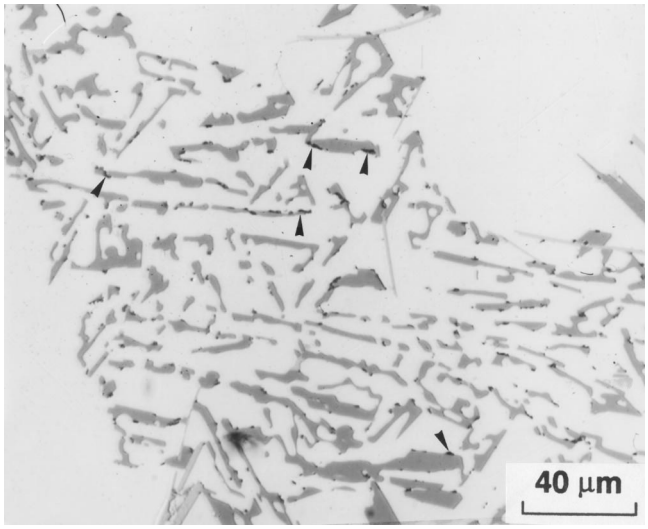


(*a*)

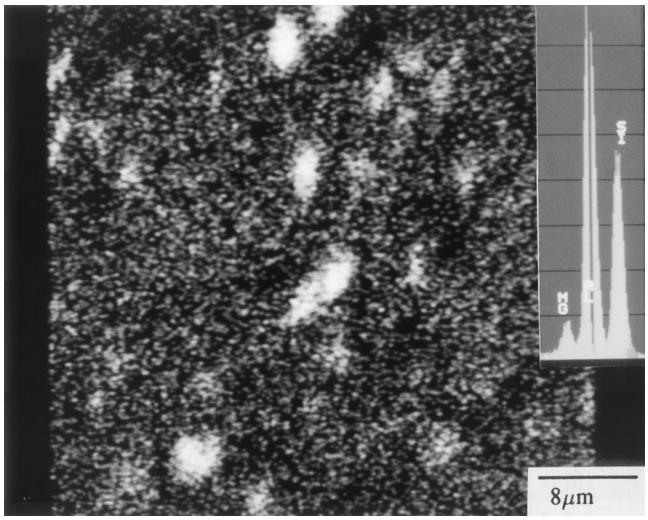


(*b*)

Fig. 13—(*a*) Optical microstructure showing precipitation of tiny black particles of $Mg_2Si$ (or Mg-rich) phase along the sides of the eutectic Si particles in 319 alloy containing less than 0.5 wt pct Mg; (*b*) X-ray image showing Mg distribution in these particles, with corresponding EDX spectrum shown in the inset.

2. *Precipitation of $Mg_2Si$*

When magnesium was added in small quantities (less than 0.5 wt pct), it was observed that tiny dark particles of $Mg_2Si$ (or an Mg-rich) phase precipitated along the long sides of partially modified eutectic Si particles, as shown by the arrows in Figure 13(a). The X-ray image given in Figure 13(b) reveals that these rounded particles are rich in Mg. The associated EDX spectrum shown in the inset exhibits a measurable Mg intensity, with the strong Si peak observed being mostly related to the presence of the eutectic Si particles underneath the $Mg_2Si$ (or Mg-rich) particles.

At Mg concentrations of 1.0 wt pct or more, the $Mg_2Si$ phase precipitated in the form of black Chinese script–like particles, as indicated by the open arrow in Figure 14(a). Also, apparently in such cases, the eutectic Si particles (dark gray) appear to be unmodified by the Mg addition. The corresponding X-ray image for Mg in shown in Figure

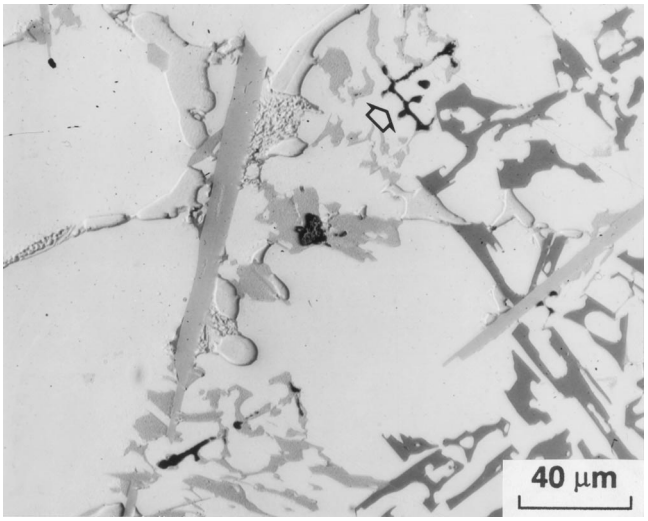


(*a*)

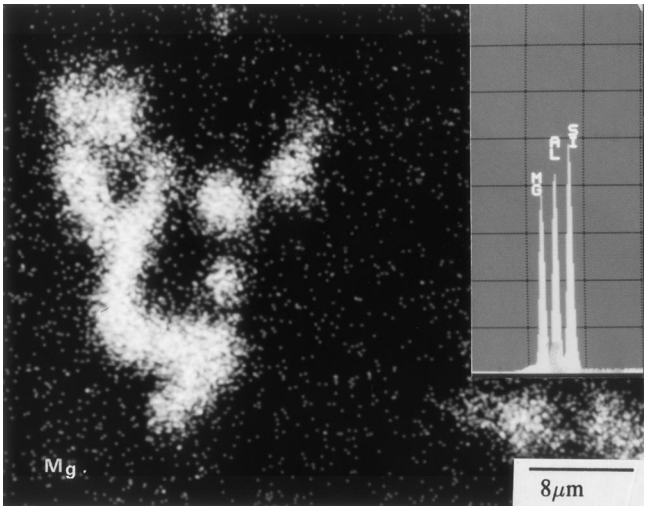


(*b*)

Fig. 14—(*a*) Optical microstructure showing precipitation of $Mg_2Si$ phase with Chinese script morphology (open arrow); (*b*) corresponding X-ray image showing Mg distribution, with EDX spectrum shown in the inset.

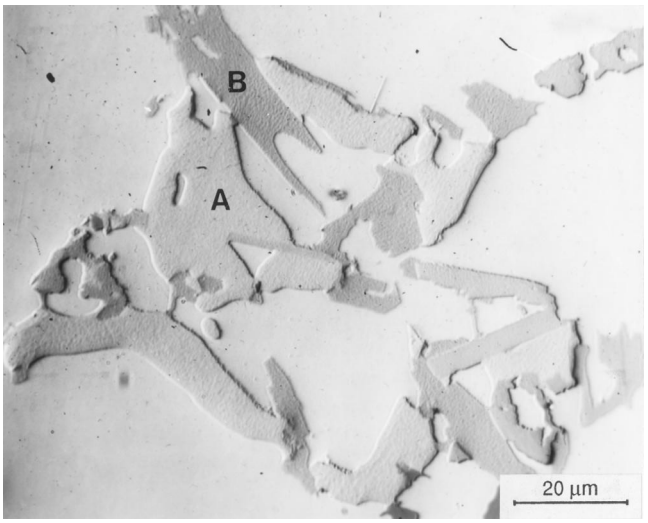


Fig. 15—Optical microstructure showing precipitation of blocklike $Al_2Cu$ (marked A) and $Al_5Mg_8Cu_2Si_6$ (marked B) phases in WMS7 alloy.

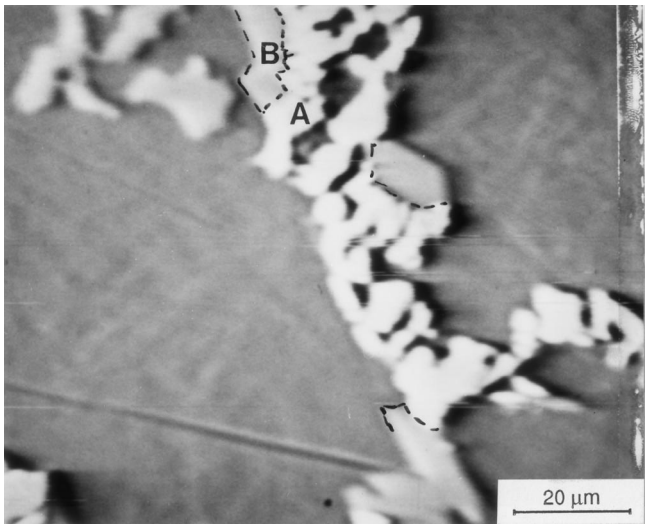


(*a*)

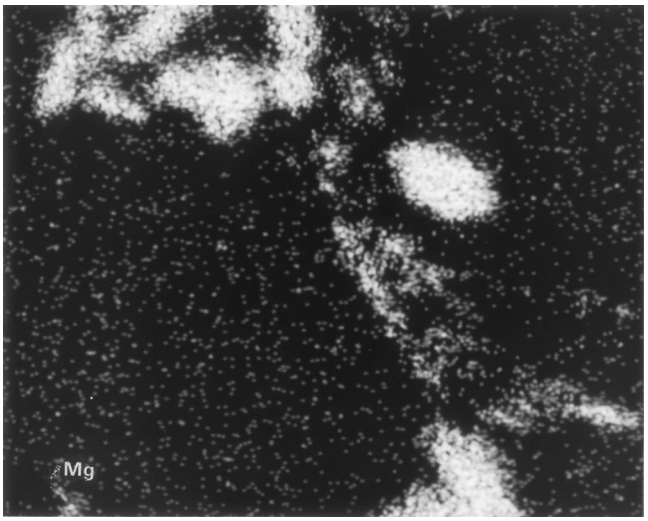


(*b*)

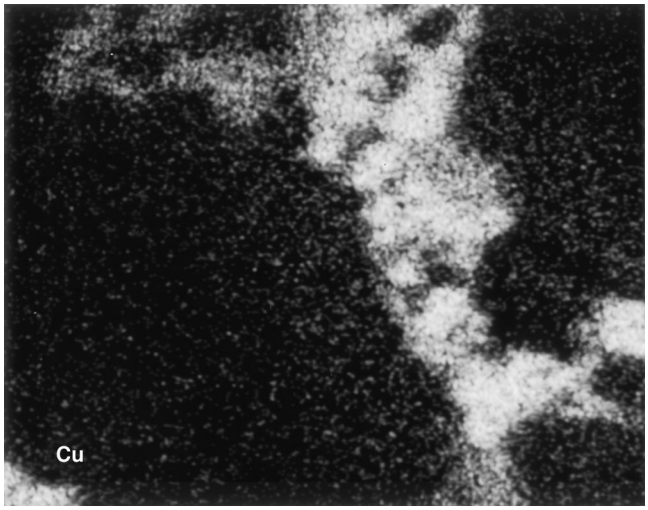


(*c*)

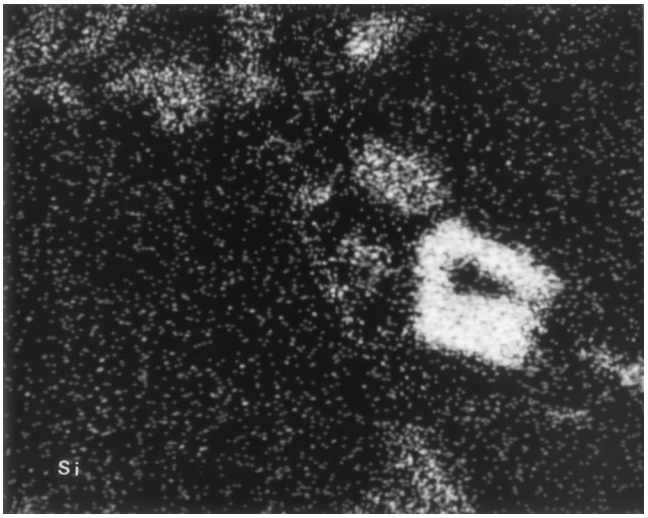


(*d*)

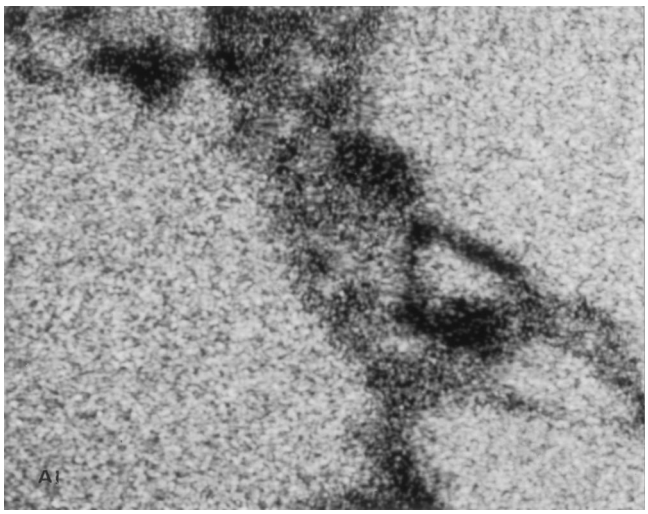


(*e*)

Fig. 16—(*a*) Backscattered image of the two copper intermetallics (A and B) taken from a particle similar to that depicted in Fig. 15, and X-ray images showing (*b*) Mg, (*c*) Cu, (*d*) Si, and (*e*) Al distributions in the two intermetallics.

14(b), where the EDX spectrum shown in the inset reveals almost equal intensities for Mg and Si compared to those shown in Figure 13(b).

3. *Precipitation of copper intermetallics*

In Mg-containing Al-Si-Cu alloys, the $Al_5Mg_8Cu_2Si_6$ intermetallic phase is reported to grow out from the $Al_2Cu$-

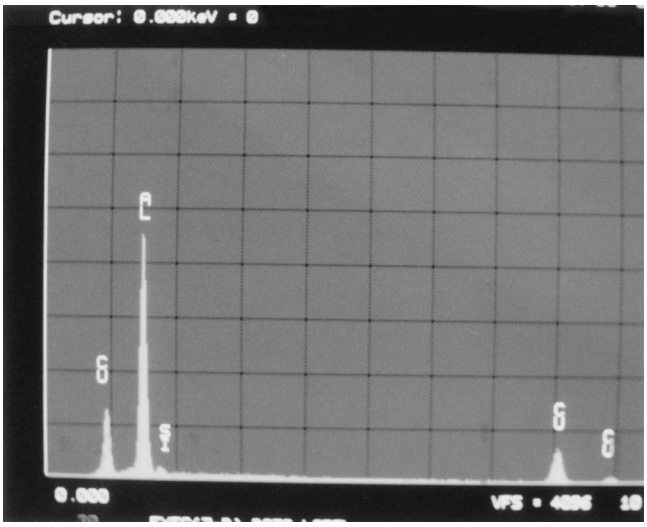


(*a*)

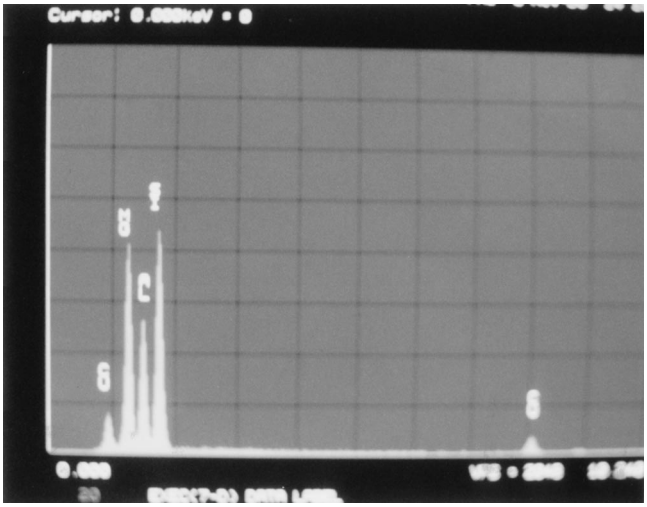


(*b*)

Fig. 17—EDX spectra corresponding to (*a*) $Al_2Cu$ and (*b*) $Al_5Mg_8Cu_2Si_6$ phases.

phase particles during the final complex eutectic reaction that takes place toward the end of solidification. An example of this is shown in Figure 15, for the WMS7 alloy sample (the secondary A319.1 alloy with Mg + Sr additions), where A and B denote the $Al_2Cu$ and $Al_5Mg_8Cu_2Si_6$ particles, respectively.

Figure 16(a) shows the backscattered image obtained from a particle similar to that shown in Figure 15, where A and B mark the two copper intermetallics, as before. The atomic weight of Cu being higher than that of Mg, the $Al_2Cu$ phase (A) appears brighter than the $Al_5Mg_8Cu_2Si_6$ phase (B) in the figure. The corresponding X-ray image for Mg is shown in Figure 16(b), where most of the Mg is found to be concentrated in the $Al_5Mg_8Cu_2Si_6$-phase particles. The X-ray image for Cu (Figure 16(c)) shows that Cu is more densely distributed in the $Al_2Cu$ phase than in the latter. From the chemical formulas, the Cu concentration in the two phases is expected to be around 33 and 9.5 pct, respectively. The Si distribution is given in Figure 16(d), showing a noticeable concentration in the $Al_5Mg_8Cu_2Si_6$ phase (apart, obviously, from that exhibited by the eutectic Si particle to its right), whereas the X-ray image for Al (Figure 16(e)) covers the surrounding matrix, as expected.

The EDX spectra for the $Al_2Cu$ and $Al_5Mg_8Cu_2Si_6$ phases are shown in Figure 17. From a quantative analysis of at least four particles in each case, the results listed in Table VII show that the element concentrations are very close to their stoichiometric compositions.[2] Elemental analysis of the various iron intermetallics shown in previous figures was similarly carried out, and the results are included in Table VII.

## IV. CONCLUSIONS

1. The addition of Mg, in amounts up to 0.5 wt pct, to molten 319-type alloys leads to the precipitation of $Mg_2Si$ (or an Mg-rich) phase that appears in the form of rounded black particles dotted along the sides of the eutectic Si particles. Noticeable fragmentation of the eutectic Si, *i.e.*, its modification, and transformation of a large proportion of the $\beta$-$Al_5FeSi$ needlelike/plateletlike phase into a Chinese script–like phase, with a composition close to $Al_8Mg_3FeSi_6$, is also observed.
2. At high levels of Mg, >1.0 wt pct, the $Mg_2Si$ precipitates in the form of black Chinese script–like particles, with a close-to-stoichiometric composition. As most of the magnesium is consumed in the precipitation of $Mg_2Si$ and $Al_8Mg_3FeSi_6$ phases, its modification effect with respect to the eutectic Si is apparently lost. At this level of Mg content, $\beta$-$Al_5FeSi$ needles are very rarely observed in the microstructure.
3. Apart from full modification of the eutectic Si, the addition of Sr, on the order of 0.02 to 0.04 wt pct, leads to the dissolution of more than two-thirds of the $\beta$ needles in the alloy matrix and modification of the $Mg_2Si$ particles. However, it does not cause nucleation of the starlike $Al_{15}(Fe,Mn,Cr)_3Si_2$ phase through transformation of the $\beta$-$Al_5FeSi$ needles. The starlike phase forms in alloys having: (1) an Fe:Mn ratio of 2:1, (2) a Cr content >0.05 wt pct, and (3) a sludge factor ≥1.8.
4. The presence of Sr results in severe segregation of the iron and copper intermetallics (except for the $\beta$-$Al_5FeSi$ needles) in areas away from the modified eutectic Si. Consequently, the Cu concentration in the $Al_2Cu$ phase can reach 40 wt pct, in which case it precipitates in the blocklike form, which is rather difficult to dissolve during solution treatment.
5. The effect of a 1.2 wt pct Mg addition in reducing the volume fraction of $\beta$-$Al_5FeSi$ needles is the same as that obtained with a 0.5 wt pct Mg + 0.03 wt pct Sr addition. In the first case, all $\beta$ needles are transformed into the $Al_8Mg_3FeSi_6$ scriptlike phase, whereas in the second, both dissolution of the $\beta$ needles in the aluminum matrix, as well as their transformation into the $Al_8Mg_3FeSi_6$ intermetallic, take place.

## ACKNOWLEDGMENTS

Financial and in-kind support received from the Natural Sciences and Engineering Research Council of Canada (NSERC), Centre Québécois de recherche et de dévelop-

pement de l'aluminium (CQRDA), General Motors Corporation, and KB Alloys, Inc. is gratefully acknowledged.

## REFERENCES


1. G.K. Sigworth, S. Shivkumar, and D. Apelian: *AFS Trans.*, 1989, vol. 97, pp. 811-24.
2. L. Backerud, G. Chai, and J. Tamminen: *Solidification Characteristics of Aluminum Alloys, Vol. 2: Foundry Alloys*, AFS/Skanaluminium, Des Plaines, IL, 1990, pp. 71-229.
3. A.M. Samuel, J. Gauthier, and F.H. Samuel: *Metall. Mater. Trans. A*, 1996, vol. 27A, pp. 1785-98.
4. S. Murali, K.S. Raman, and K.S.S. Murthy: *Mater. Characterization*, 1994, vol. 33, pp. 99-112.
5. J. Gobrecht: *Giesserei*, 1976, vol. 63, pp. 558-61.
6. L.R. Morris and F.B. Miners: U.S. Patent No. 3, 926, 690, 1975.
7. M.H. Mulazimoglu, A. Zaluska, J.E. Gruzleski, and F. Paray: *Metall. Mater. Trans. A*, 1996, vol. 27A, pp. 929-36.
8. F.H. Samuel and A.M. Samuel: *Proc. Int. Symp. on Light Metals 1997*, 36th Annual Conference of Metallurgists of CIM, Sudbury, ON, Aug. 17–20, 1997, pp. 425-37.
9. A. Pennors, A.M. Samuel, F.H. Samuel, and H.W. Doty: *AFS Trans.*, 1998, vol 106, paper no. 98-105, in press.
10. A.M. Samuel, H.W. Doty, and F.H. Samuel: *J. Mater. Sci.*, 1996, vol. 31, pp. 5529-39.
11. J.E. Gruzleski and B.M. Closset: *The Treatment of Liquid Aluminum-Silicon Alloys*, American Foundrymen's Society, Inc., Des Plaines, IL, pp. 25-126.
12. J. Sakwa: *Giesserei-Forschung*, 1986, vol. 38, pp. 112-18.
13. S. Bercovici: ''Control of Solidification Structure and Properties of Al-Si Alloys,'' Presentation at 45th International Foundry Congress, 1978.
14. H. de la Sablonniere and F.H. Samuel: *Int. J. Cast Met. Res.*, 1996, vol. 9 (4), pp. 195-211 and pp. 213-25.
15. P. Ouellet: Master's Thesis, UQAC, Chicoutimi, 1997.
16. L.F. Mondolfo: *Aluminum Alloys: Structure and Properties*, Butterworth and Co., London, 1978, pp. 759-65.
17. A.M. Samuel and F.H. Samuel: *Int. J. Cast Met. Res.*, 1997, vol. 10, pp. 147-57.
18. S.C. Flood, P.V. Evans, J.M. Brown, and J. Worth: in *Light Metals 1995*, J. Evans, ed., TMS, Warrendale, PA, pp. 1127-35.
19. S.G. Shabestari: Ph.D. Thesis, McGill University, Montreal, 1995.
20. D.A. Granger: *AFS Trans.*, 1991, vol. 99, pp. 379-83.